

## Selective laser melting of AlSi10Mg

Tradowsky, U.; White, J.; Ward, R. M.; Read, N.; Reimers, W.; Attallah, M. M.

DOI:

[10.1016/j.matdes.2016.05.066](https://doi.org/10.1016/j.matdes.2016.05.066)

License:

Creative Commons: Attribution-NonCommercial-NoDerivs (CC BY-NC-ND)

*Document Version*

Peer reviewed version

*Citation for published version (Harvard):*

Tradowsky, U, White, J, Ward, RM, Read, N, Reimers, W & Attallah, MM 2016, 'Selective laser melting of AlSi10Mg: Influence of post-processing on the microstructural and tensile properties development', *Materials and Design*, vol. 105, pp. 212-222. <https://doi.org/10.1016/j.matdes.2016.05.066>

[Link to publication on Research at Birmingham portal](#)

### General rights

Unless a licence is specified above, all rights (including copyright and moral rights) in this document are retained by the authors and/or the copyright holders. The express permission of the copyright holder must be obtained for any use of this material other than for purposes permitted by law.

- Users may freely distribute the URL that is used to identify this publication.
- Users may download and/or print one copy of the publication from the University of Birmingham research portal for the purpose of private study or non-commercial research.
- User may use extracts from the document in line with the concept of 'fair dealing' under the Copyright, Designs and Patents Act 1988 (?)
- Users may not further distribute the material nor use it for the purposes of commercial gain.

Where a licence is displayed above, please note the terms and conditions of the licence govern your use of this document.

When citing, please reference the published version.

### Take down policy

While the University of Birmingham exercises care and attention in making items available there are rare occasions when an item has been uploaded in error or has been deemed to be commercially or otherwise sensitive.

If you believe that this is the case for this document, please contact [UBIRA@lists.bham.ac.uk](mailto:UBIRA@lists.bham.ac.uk) providing details and we will remove access to the work immediately and investigate.

# **Selective Laser Melting of AlSi10Mg: Influence of Post-Processing on the Microstructural and Tensile Properties Development**

**U Tradowsky<sup>1</sup>, J White<sup>2</sup>, R.M Ward<sup>2</sup>, N Read<sup>2</sup>, W Reimers<sup>3</sup>, MM Attallah<sup>2§</sup>**

1. Photon Laser Engineering, Photon AG, Staakener Str. 53-63, D-13581 Berlin, Germany.
2. School of Metallurgy and Materials, University of Birmingham, Edgbaston, Birmingham, B15 2TT, UK.
3. Fachgebiet Metallische Werkstoffe, Institut für Werkstoffwissenschaften, Technische Universität Berlin, , Ernst-Reuter-Platz 1, D-10587 Berlin, Germany.

§Corresponding author: Email: M.M.Attallah@Bham.ac.uk, Tel. : +44 121 4147842, Fax: +44 121 4147890

# **Selective Laser Melting of AlSi10Mg: Influence of Post-Processing on the Microstructural and Tensile Properties Development**

## **ABSTRACT**

The study looks into the impact of thermal post-processing using Hot Isostatic Pressing (HIPping) and/or T6-peak aging treatment, post-process machining, as well as the build orientation on the microstructural and mechanical properties development in AlSi10Mg alloy fabricated using Selective Laser Melting (SLM). The builds contained fine columnar grains, with a fine Si-enriched cellular dendritic network, resulting in tensile strengths exceeding the castings. To elucidate the as-fabricated microstructure and strength, thermal modelling was employed, predicting cooling rates of  $10^5$ - $10^6$  °C/s.

Voids, mostly due to oxide films, were observed using Micro-CT in the as-fabricated condition. HIPping collapsed most voids, showing virtually no trace even after a further T6 treatment. Generally, the tensile properties of the majority of conditions were significantly better than in the cast+T6 equivalent alloy. Post-process machining was also found to improve the strength (compared to the as-fabricated surface). However, HIPping+T6 allowed the builds to achieve the required tensile properties, without surface machining. By assessing the influence of powder recycling, it was found that the void content linked to oxide layer formation increased following powder recycling, resulting in a drop in tensile properties. The interaction between the microstructure, surface condition, thermal post-processing, and fracture mode is discussed.

**Keywords:** Aluminium Alloys; Selective Laser Melting; Microstructure; Tensile Properties

## I-INTRODUCTION

Additive layer manufacturing (ALM) is on the rise, making the step from rapid prototyping and rapid tooling to manufacturing applications [1]. Different technologies are employed, electron beam melting (EBM), direct laser fabrication (DLF) and selective laser melting (SLM). With AM, very complex structures with integrated functionalities can be made. This can be used further for reducing the weight of components, leading to cost reduction over the life span [2]. Interest into ALM of various advanced metallic materials such as Ni superalloys and Ti alloys has increased over the last decade [3–6]. Al alloys are of major interest for lightweight applications in aerospace and automotive sector. AlSi10Mg is an age-hardenable cast alloy with good mechanical properties. Castability and weldability is good due to the composition being close to eutectic Al-Si. Age hardening is enabled by Mg, which raises strength by  $Mg_2Si$  precipitation sequence. Due to these reasons, AlSi10Mg is a good candidate for SLM. Process parameters [7,8], resulting microstructure and mechanical properties have already been under thorough research for this alloy [9–12]. However, no work that considered comprehensively within the same study the influence of post-processing, machining, thermal treatments, and the influence of powder recycling on the mechanical properties of AlSi10Mg, is present in the literature. Considering all these factors within the same study avoids the cross-studies inconsistencies due to the variation in the powder feedstock, processing conditions, or SLM platform type.

For cast AlSi10Mg, solution heat treatment followed by artificial aging heat treatment (T6) is the standard post-processing to achieve best mechanical properties [13,14]. Hot Isostatic Pressing (HIPping) of cast material is typically employed to ‘heal’ some of the casting defects such as shrinkage porosity [15]. Combinations of T6 with HIPping were found to improve the

mechanical properties of cast Al-alloys, as the HIPping improves fatigue life and the T6 heat treatment achieves good yield strength (YS) and ultimate tensile strength (UTS) [16].

This paper aims at assessing the impact of thermal post-processing on the microstructural and mechanical properties development in SLMed AlSi10Mg alloy. Furthermore, recycled powder has been used to establish the impact on mechanical properties of Al alloy SLM for the first time, since powder recycling has been investigated previously only for Ni and Ti alloys [17–19]

## II. MATERIALS AND METHODS

### *II.a. Material*

The powder used in this study was gas atomised AlSi10Mg supplied by TLS Technik. The composition is shown in Table 1. Fig. 1a shows a Scanning Electron Microscope (SEM) micrograph of the powder. The morphology is spherical. Fine satellite particles ( $<5\mu\text{m}$ ) are found attached to the larger particles. The coarse particles also show a rougher (dendritic) surface compared with the smooth surface of all small ( $<30\mu\text{m}$ ) particles. The cross section micrograph (Fig. 1b) reveals no internal (entrapped gas) porosity or other defects. The 10%, 50% and 90% points of the size range distribution were  $15\mu\text{m}$ ,  $34\mu\text{m}$  and  $55\mu\text{m}$  respectively (Fig. 1c). This was measured using a Helos laser diffraction unit. The flowability, as measured using the Schulze ring test [20], was found to give a Flow Factor Classification (FFC) of 10.35, and the ratio of the tap to apparent densities (Hausner ratio),  $H = \frac{\rho_{\text{tap}}}{\rho_{\text{bulk}}}$  was 1.29, which are both indicative of a good powder spreading behaviour, as required for SLM [21,22].

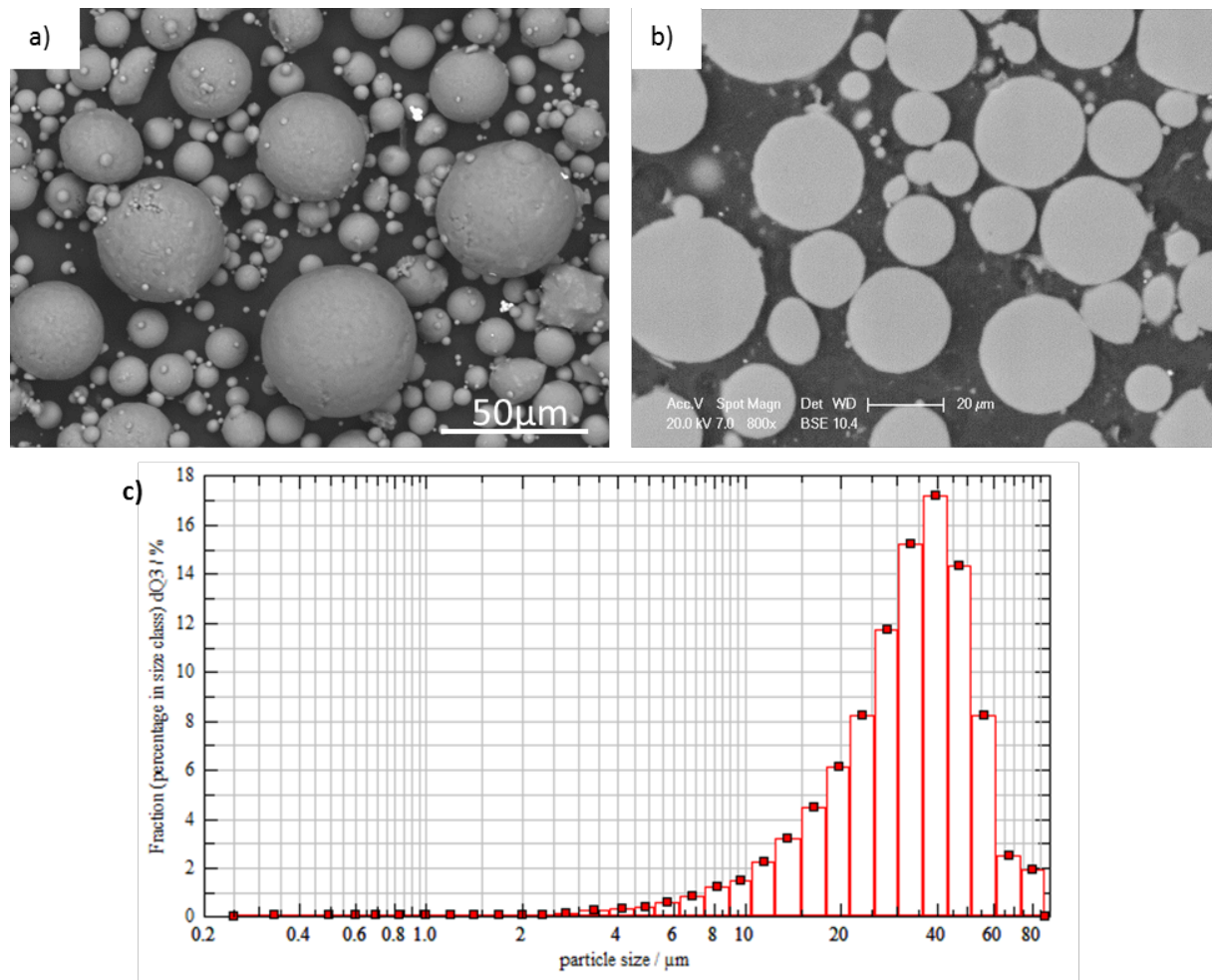


**Fig. 1.** AlSi10Mg powder with +25-50µm size range: a) SEM micrograph showing the powder morphology, b) SEM cross-section micrograph for the sectioned powder particles (showing no internal porosity), and c) powder size distribution.

**Table 1.** Chemical composition of AlSi10Mg powder

Element	Al	Si	Mg	Fe	Mn	Cu	Zn	Ti	Ni	Total
Nominal composition (wt. %)	Bal.	10.2	0.3	0.15	0.05	0.005	<0.002	0.015	0.012	100

## *II.b. SLM*

All specimens were fabricated using a Concept Laser M2 Cusing system (laser powder-bed fusion). The M2 system has an Yb-fibre laser with a laser power up to 400 W and a 60 µm laser spot size. All processing was carried out in an Argon atmosphere with an Oxygen

content below 0.1%. A “chess scanning strategy” was used in fabricating the specimens, in which the filled layer is divided into several 5.6 mm square (islands) with each island being built randomly and continuously. Inside each island, the laser is raster-scanned individually. After selective melting the islands, laser scans are carried out around the perimeter of the layer to improve the surface finish. For each subsequent layer, these islands are translated by 1 mm in the X and Y-directions and the scanning direction inside the islands is changed by 90°. Samples were processed in two orientations. Vertically built samples have their long axis orientated parallel to the building direction, horizontally built samples are orientated normal to the building direction, Fig. 2.

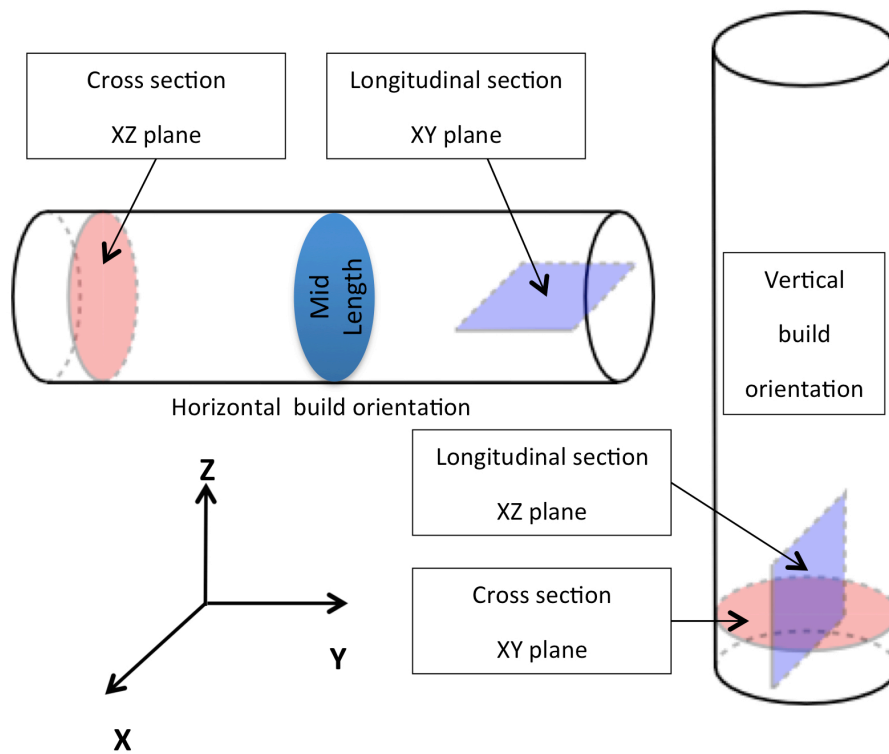


**Fig.2.** Building orientations and sectioning for microscopy

The following parameters were used: 175 W power, 1025 mm/s scan speed, layer thickness of 30  $\mu\text{m}$ , and 97.5  $\mu\text{m}$  scan spacing, based on the optimum parameters indicated in a previous study [7]. It is important to mention that the previous study [7] optimised the process

parameters for non-spherical powders, compared to the powders examined in the current study, meaning that the parameters are unlikely to be transferable (i.e. giving full consolidation). However, as the aim of the current study is to assess the impact of post-processing rather than the parameters, the selected parameters were acceptable.

### *II.c. Post-Processing*

HIPping was performed using an EPSI HIPping vessel. For the solution treatment + peak aging heat treatments (T6), an electrically heated furnace from LTD was used. Table 2 shows the post-processing parameters used in this study.

**Table. 2** HIPping and T6 Heat Treatment Parameters

HIPping Parameters			
Temperature	Pressure	Time	Heating- / Cooling Rate
530°C	100MPa	2h	5°C/min
T6 Parameters			
Solution HT		Aging HT	
520°C/5h/Water quenching		160°C/12h/air cooling	

### *II.d. Specimen Machining*

Table 3 and Fig. 3 show the number and geometry of the specimens used for mechanical testing. Some dogbone specimens had the M6 thread built into them using SLM, and then later die-threaded, with the gauge part of the dogbone specimens sand blasted (denoted R). Sand blasting was applied to remove residual (partially-molten) powder particles from the surface, which is a standard procedure in industrial SLM operations to improve the surface finish. Other samples were built as rod, and machined to M6 dogbone geometry (denoted M).



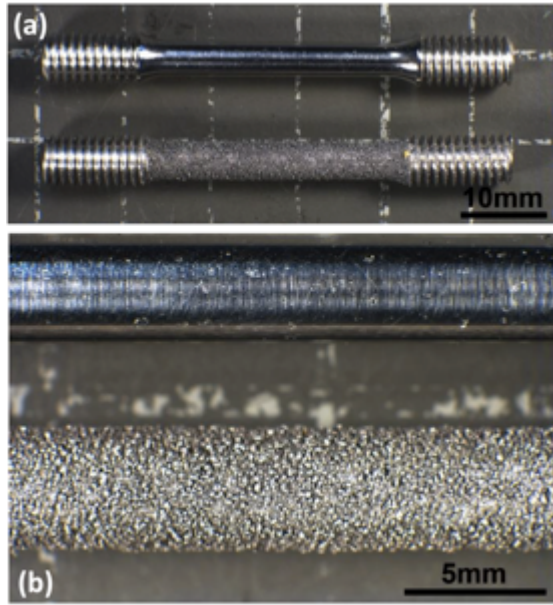


**Fig. 3.** The geometry of the mechanical testing specimens; (a) the machined specimen (top) and the as-built surface with die-engraved threads (bottom), and (b) a close-up macrograph for the specimens surfaces.

**Table 3.** A summary of the conditions investigated using tensile testing

<i>Vertical Build Orientation (V)</i>		
Condition	Machined from rod (M)	As-fabricated Dogbone (rough surface, R)
As-fabricated (AF)	3 (AF-V-M)	3 (AF-V-R)
HIP-only (HIP)	3 (HIP-V-M)	3 (HIP-V-R)
T6-only (T6)	3 (T6-V-M)	3 (T6-V-R)
HIP plus T6 (HIP+T6)	3 (HIP+T6-V-M)	3 (HIP+T6-V-R)
As-fabricated fresh powder (FP)	3 (AF-V-M-FP)	-
As-fabricated recycled powder (RP)	3 (AF-V-M-RP)	-
<i>Horizontal Build Orientation (H)</i>		
Condition	Machined from rod (M)	As-fabricated Dogbone (rough surface, R)
As-fabricated (AF)	3 (AF-H-M)	3 (AF-H-R)
HIP-only (HIP)	3 (HIP-H-M)	2 (HIP-H-R)
T6-only (T6)	3 (T6-H-M)	3 (T6-H-R)
HIP plus T6 (HIP+T6)	3 (HIP+T6-H-M)	3 (HIP+T6-H-R)

### *II.e. Tensile Testing*

A servo-hydraulic Zwick/Roell tensile testing machine with an external extensometer, operated using TestExpert II software (v 3.1), was used for tensile testing. All tests were carried out at room temperature in accordance to BS EN ISO 6892-1:2009 and ASTM E8/E8M [23,24], testing three samples per condition as appropriate.

### *II.f. Optical and Electron Microscopy*

For the vertically-built samples, a dogbone specimen was sectioned at 5 mm from the bottom of samples to observe the cross sections (XY plane). For the horizontally built samples, a dogbone specimen was sectioned at mid-length (y-direction, Fig. 2) to observe the cross-section. The longitudinal section was taken from the lower end of vertically built samples to be comparable in built height with the horizontally built samples. To observe the microstructure, the sectioned samples were mounted in bakelite and polished down to a 0.05  $\mu\text{m}$  finish for microstructure observation. A Zeiss Axioscope microscope was used at 200x magnification to analyse the voids in all conditions. Image J (v1.48) was used to quantify the number of voids.

Polished specimens were etched by immersion in a NaOH solution for 10-60s to reveal the melt pool microstructure. To reveal the grain structure, the as-fabricated and HIP+T6 specimens were electrolytically etched using Barker's reagent (5ml  $\text{HBF}_4$  in 200ml  $\text{H}_2\text{O}$ ) for 60s at 20V. A polarised light OM (Leica DMRX) used to examine the melt pool and grain structure of the as-fabricated and HIP+T6 conditions. A Philips XL30 scanning electron microscope, equipped with Oxford INCA energy dispersive X-ray spectroscopy (EDX) detector, was used for imaging of the microstructure for observation of all conditions and to analyse the fracture surfaces.

### *II.g. X-Ray Micro Computed Tomography*

A Bruker Skyscan 1172 X-ray micro-tomography ( $\mu\text{CT}$ ) X-ray machine was used to scan the as-fabricated condition. The scan was performed at 80kV, 100 $\mu\text{A}$ , with an Al+Cu filter and an object to source distance of 40.8 mm. Images were taken every 0.13, yielding a voxel size of

1.69  $\mu\text{m}$ . Reconstruction was performed using NRecon software, performing an optimisation for smoothing, beam hardening, ring artefacts and post alignment correction. Image analysis and thresholding were performed in CTan software, whereby the binary images were separated according to volume and split into individual .STL files for visualisation purposes.

### *II.h. Numerical modelling*

A 3D heat transfer model using approximately 20M elements of  $(19.5 \mu\text{m})^3$  on an  $8 \text{ mm} \times 8 \text{ mm} \times 5 \text{ mm}$  region was created and solved using an explicit finite difference formulation. It is recognised that excluding fluid flow will affect the accuracy of the model, but with the bonus of permitting a larger volume to be simulated (see Khairallah et al., [25] for a detailed discussion of the effects). The thermophysical properties were obtained from the literature [26] with the quoted latent heat of fusion evenly distributed across the solidification range and added on to the specific heat data there. As these property data are for a casting simulation, they are likely to exclude the effects of rapid cooling on the enthalpy-temperature-phase relationship [27]. At high cooling rates the time required for nucleation and/or growth during solidification can decrease the liquidus and solidus temperatures, and potentially permit liquid to supercool below the solidus before solidifying and releasing latent heat (recalescence). Therefore the model results should be treated as approximations.

## **III. RESULTS AND DISCUSSION**

### *III.a. Voids*

Quantitative analysis of the porosity development in the as-fabricated and T6-only vertical samples using OM and  $\mu\text{CT}$  showed porosity levels  $\sim 1\text{-}2\%$ , Fig. 4. The build contained irregular shaped voids, with sizes up to several 100  $\mu\text{m}$  and elongated normal to the build direction, Fig. 5, Fig. 6 and Fig. 7. The results show that the measurement of the void content

along the build direction usually yields higher values compared with the cross-section (Fig. 4), because the voids are mainly orientated with their long axis perpendicular to building direction.

The longitudinal measurements however agreed with the measurement obtained using  $\mu$ CT (Fig. 5). The results also show that the samples with the uniform geometry (AF-V-M-FP) showed lower void content compared with the sample built with a threaded end (AF-V-R).

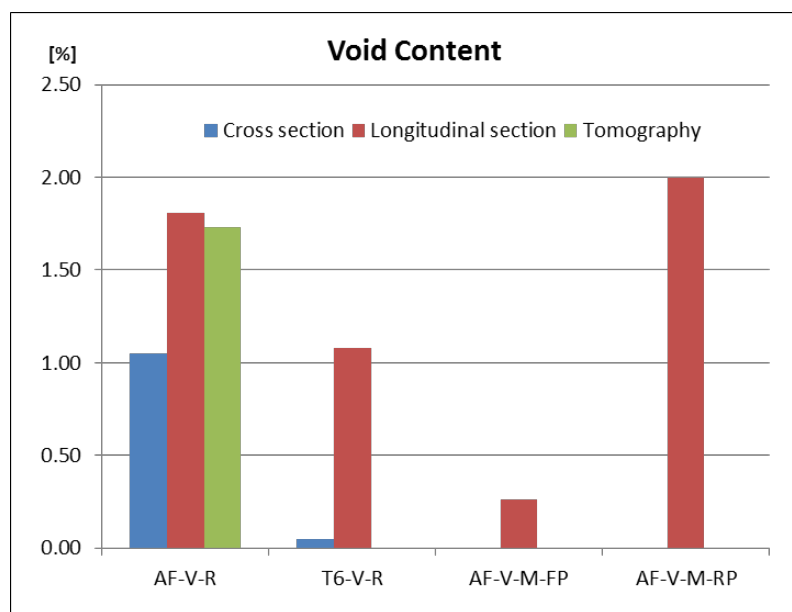


**Fig. 4.** The development of the void content in the vertical build orientation in the as-fabricated dogbone (AF-V-R), T6 only (T6-V-R), as-fabricated from fresh powder rod (AF-V-M-FP), and the as-fabricated from recycled powder rod (AF-V-M-RP), showing a comparison between  $\mu$ CT, and optical measurements in the plane along and transverse to the build direction.

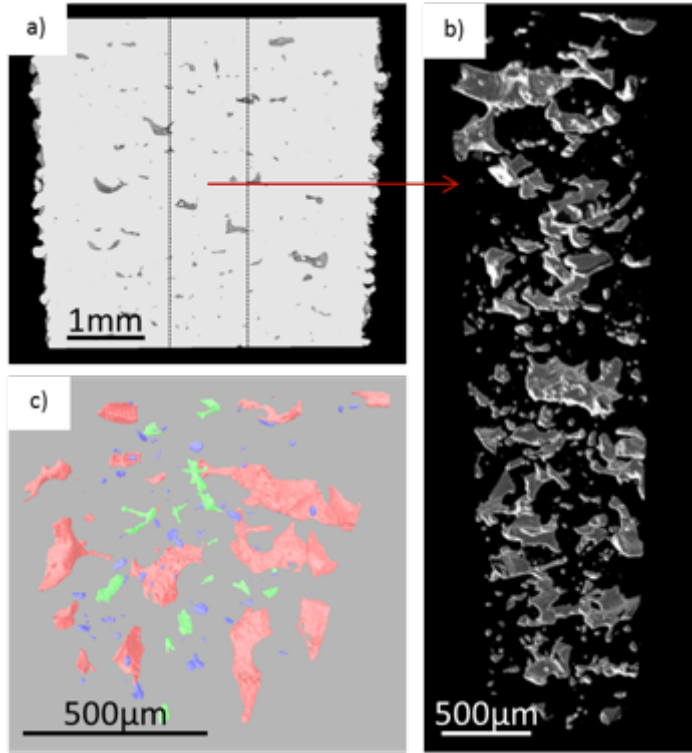


**Fig. 5.**  $\mu$ CT image of the vertically built as-fabricated sample, showing a) longitudinal section of volume data reconstructed from 2D images, showing void distribution; b) voids only from a cylindrical region taken from the centre of the reconstructed volume (diameter of the centre section=1mm, shown by dashed lines in (a); and c) different void sizes in the sample taken from the centre of the reconstructed volume (height = 1 mm, diameter = 1 mm, shown by dashed lines in Fig.5.a) spherical voids are shown in blue, the elongated fine voids in green, and the large voids in red. The voxel size is 1.7  $\mu$ m, threshold voxel volumes were set at <500vx (blue), 500-5000vx (green), >5000vx (red).

Furthermore, the samples processed using recycled powder showed significantly more voids than the samples processed using fresh powder (2% and 0.26% respectively, Fig. 4 and Fig. 5).

The irregular surface of each SLM layer, combined with the presence of oxide films, provides resistance to re-melting across the meltpools. In the regions where the localised powder layer exceeds the deposited layer thickness, the laser provides insufficient energy to allow the pool to penetrate evenly through to the substrate. Similarly, the oxide layer can inhibit the penetration of the melt and disrupts wetting. The melt bridges the area forming a void in the region across the layer.

The irregular shaped voids are caused by oxide film formation. Due to high reactivity of Al with Oxygen, it is likely that the surface of the powder particles becomes enriched in Oxygen during recycling (e.g. via moisture) or during fabrication through the formation of an oxide film on the meltpool surface of each layer. When re-melting occurs in the subsequent layer(s), the laser power may not be sufficient to remelt the oxide ( $\text{Al}_2\text{O}_3$ ), creating a void. The void surface is smooth with some waviness (Fig. 7), typical for oxides [7]. Some voids enclose unconsolidated powder (Fig. 7b), suggesting the entrapment of powders between the oxide films. EDX measurements confirm high Oxygen-content on the void surface compared to the matrix, suggesting the presence of an oxide film (Fig. 7c). Following HIPping, no open voids were observed since HIPping collapses the voids. As the main void type observed is due to oxide film, which is different from the gas entrapment pores, there was no re-opening during the subsequent T6 heat treatment. However, the oxide layers remain in the material, as the HIPping temperature is well below the melting temperature of  $\text{Al}_2\text{O}_3$  of  $2052^\circ\text{C}$  [28].

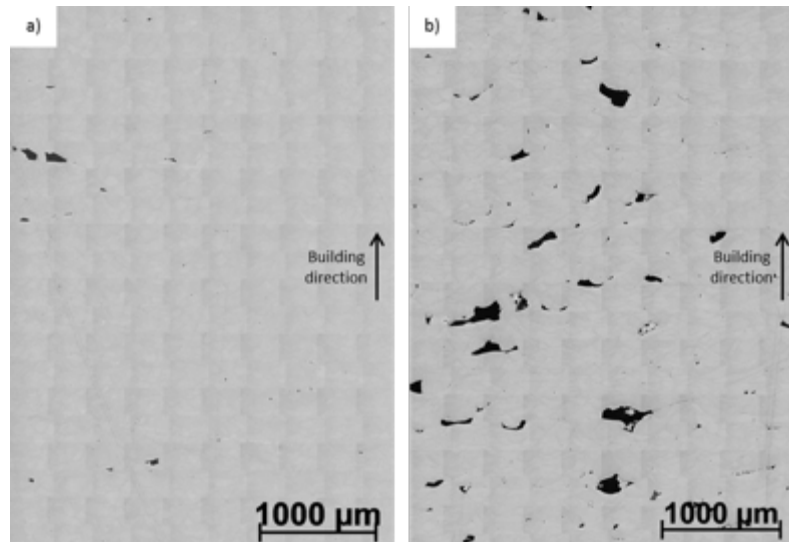


**Fig. 6.** Voids in vertically built as-fabricated samples made using a) fresh powder (0.26 % voids) and b) recycled powder (2% voids, after a single full recycling build).

The void content found in cross sections was generally lower than in the longitudinal sections. More defects are observed in longitudinal sections, as the defects are result of the layer wise processing. Cross section images only represent a small number of layers, whereas the longitudinal section represents high number of layers. However, longitudinal bridged voids can be observed in cross sections, Fig. 8.

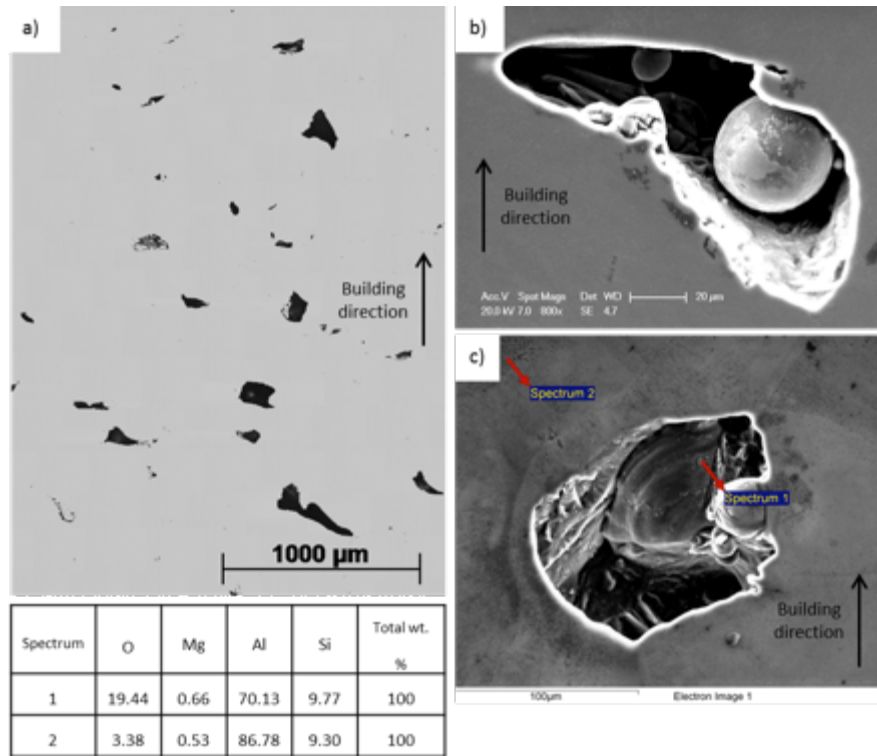


**Fig. 7.** Micrographs of voids in the as-fabricated samples, showing a) OM micrograph for the voids distribution and orientation, (b) SEM micrograph of a void with entrapped powder particles, and (c) SEM/EDX on a wavy void surface (Spectrum 1) compared against the matrix (Spectrum 2).

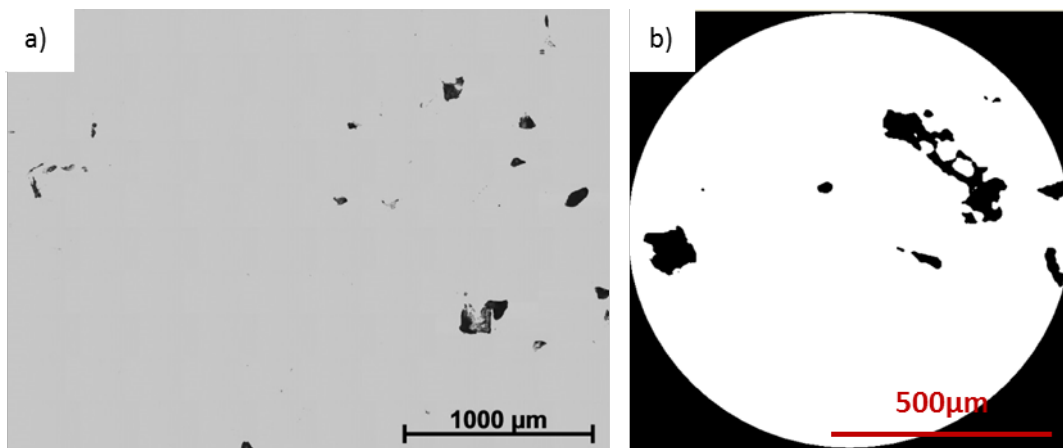


**Fig. 8.** (a) Cross section micrograph, and (b)  $\mu$ CT tomograph of vertically built as-fabricated samples. Both images show longitudinal bridged voids.

### *III.b. Meltpool and Microstructure*



The cross section of the as-fabricated sample revealed meltpool patterns with interwoven scan tracks similar to the scan strategy, Fig. 9a, and with the typical fish-scale along the build direction. The interlayer meltpool depth, measured as the maximum thickness of the fish-scale morphology along the build direction, occasionally varied between 50 to 130  $\mu\text{m}$ , Fig. 9b and Fig. 9d. Since the powder layer thickness was 30  $\mu\text{m}$ , this suggests the presence of significant yet inconsistent re-melting across the layers during SLM. The interlayer meltpool width (as observed in the cross-section, Fig 9a) can reach  $\sim 2$  times the scan spacing which shows that the laser thermal footprint exceeds the scan spacing and laser spot size ( $\sim 60 \mu\text{m}$ ). The meltpools consisted of a cellular dendritic network with cell sizes below 1  $\mu\text{m}$  (Fig. 9c). The area marked “A” corresponds to a meltpool border, where the dendrite cells are larger. The network itself is Si enriched (Spectrum 1), whereas the cells in between are depleted in Si (Spectrum 2), which was confirmed by EDX. The builds generally showed a columnar grain structure along building direction that grow across the meltpool layers, Fig. 9d. The grains show a width of  $\sim 5 \mu\text{m}$ . Grain size was difficult to quantify using OM due to the high Si-content. In the as fabricated samples, the Si-enriched cellular dendritic network overshadowing the grain boundaries.

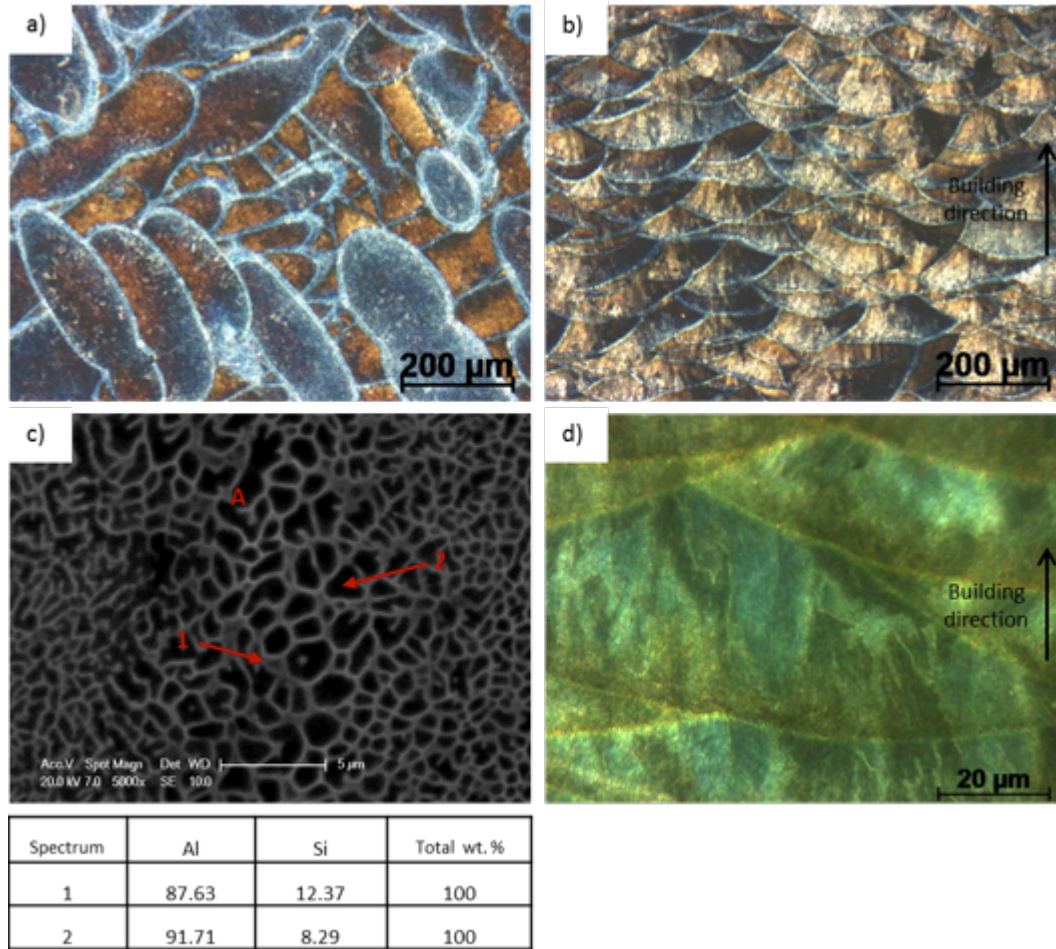


**Fig. 9.** Micrographs of the as-fabricated vertically built microstructure, showing OM micrographs for the meltpool patterns (a) cross section, (b) longitudinal, (c) SEM micrograph (XZ plane) and the corresponding EDX point analyses on the dendrite cell network, and (d) POM micrograph of the longitudinal section, showing the columnar grain structure growing across the meltpool borders along the build direction.

Post-processing resulted in homogeneous microstructures, with rounded Si particles (1-5  $\mu\text{m}$  in size) randomly scattered particles in the Al-matrix, Fig. 10. Evidence on the collapse oxide-film defects was evident in the microstructure following HIPping, Fig. 10a, maintaining the collapse following the T6 heat treatment. Furthermore, few needle  $\text{AlFeSi}$  precipitates were evident in the microstructure and confirmed by EDX (Fig. 10b), which may contribute to the strength through Orowan strengthening, although this is likely to be minor contribution due to their limited fraction (compared to the round Si-precipitates). EBSD was used to quantify the

grain size following HIPping+T6 treatment, showing a grain size of fairly similar size range to the as-fabricated condition ( $\sim 5 \mu\text{m}$ ), yet as a mixture of mainly columnar and some equiaxed grains (towards the meltpool boundary), Fig. 10c. It can be concluded, that HIPping+ T6 does not cause grain growth, possibly due to the pinning effect of the various secondary phases observed in this alloy (Si and  $\beta\text{-AlFeSi}$  particles) [29,30]. The  $\beta\text{-AlFeSi}$  precipitate was not found in HIP-only samples, as it forms during aging.

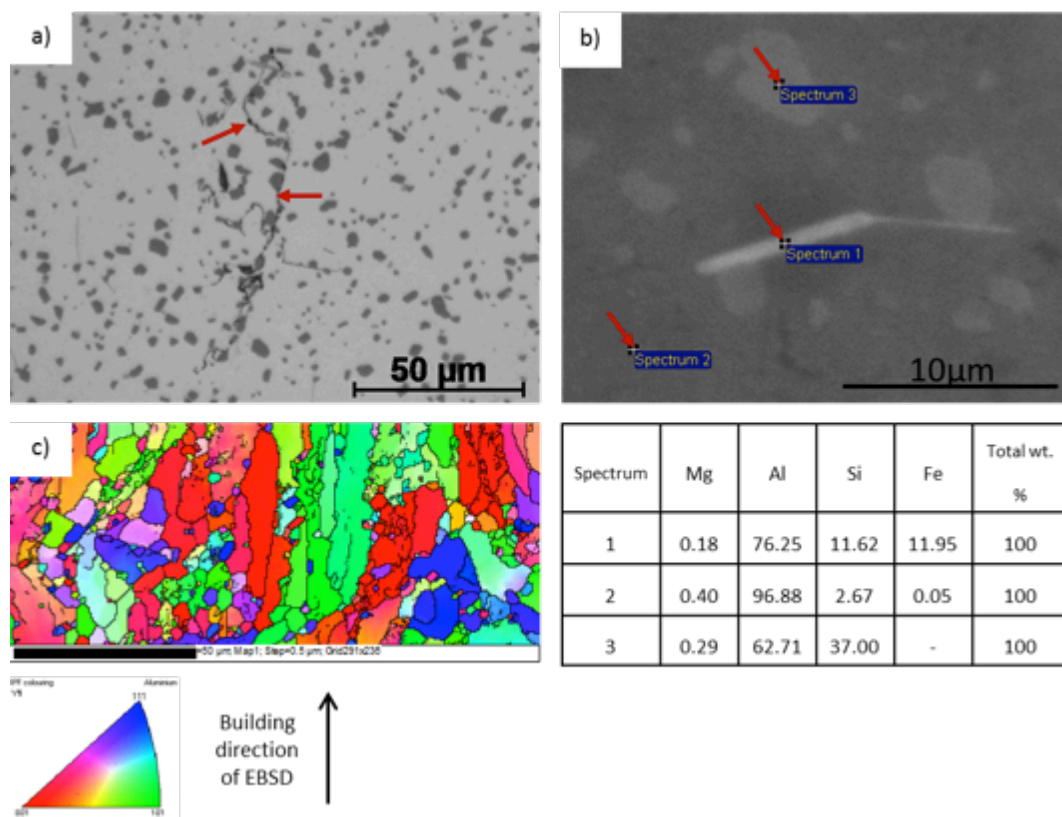


**Fig. 10.** Post-processed microstructures, showing (a) OM micrograph for HIP+T6 with Si-particles (grey) in Al-matrix (red arrows indicating a closed oxide film induced void, with the oxide layer remaining in the material), (b) SEM micrograph for the needle AlFeiSi particles (spectrum 1) and some rounded Si-particles (spectra 2 and 3) in the T6-only condition, and (c) EBSD map in the HIP+T6 condition showing a single meltpool region.

### III.c. Mechanical Properties

Horizontal SLM samples of all conditions, with the exception of the HIP-only, were found to exhibit YS and UTS at least at level of cast (T6) material, with the vertical specimens achieving the YS only (T6-V-R; T6-only, vertically built, as-fabricated surface) or up to 100MPa better (AF-H-M and -R; as-fabricated, horizontally built, machined and as-fabricated surface) (Fig. 11). This might be attributed to the finer grain sizes of about 5 $\mu$ m compared to cast alloy [31], as well as the extremely fine dendrite cell network with cell sizes below 1  $\mu$ m. Elongations of all conditions, again with the exception of the HIP only, were at level of cast alloy or slightly better. HIP-only samples showed large elongation, but lower strength compared to the T6 and HIP+T6 conditions, possibly due to the lack of precipitation strengthening. In fact, the YS and UTS in the HIP-only condition were at level of solution heat treated cast alloy [32]. Horizontally built HIP-only samples show 20% elongation and more, with the machined samples being better with lower deviation between samples (HIP-H-M and HIP-H-R). This difference in favour of the machined surface over the as-fabricated surface condition might be linked to the reduction of surface defects in machined samples.

The YS of HIP+T6 condition was higher than the YS of the as-fabricated condition and the T6-only condition (Fig. 11). This can be linked to voids being closed in the HIPped specimens, as yielding starts at defects and void defects are only found in the as-fabricated samples and T6-only samples, which show similar YS. The UTS of T6-only and HIP plus T6 samples remains below the as-fabricated samples. This is linked to the extremely fine dendritic network in the as-fabricated condition. The standard deviation of the post-processed conditions was significantly smaller than in the as-fabricated condition. This is linked to the more homogeneous microstructures after heat treatments, especially without voids after HIPping.

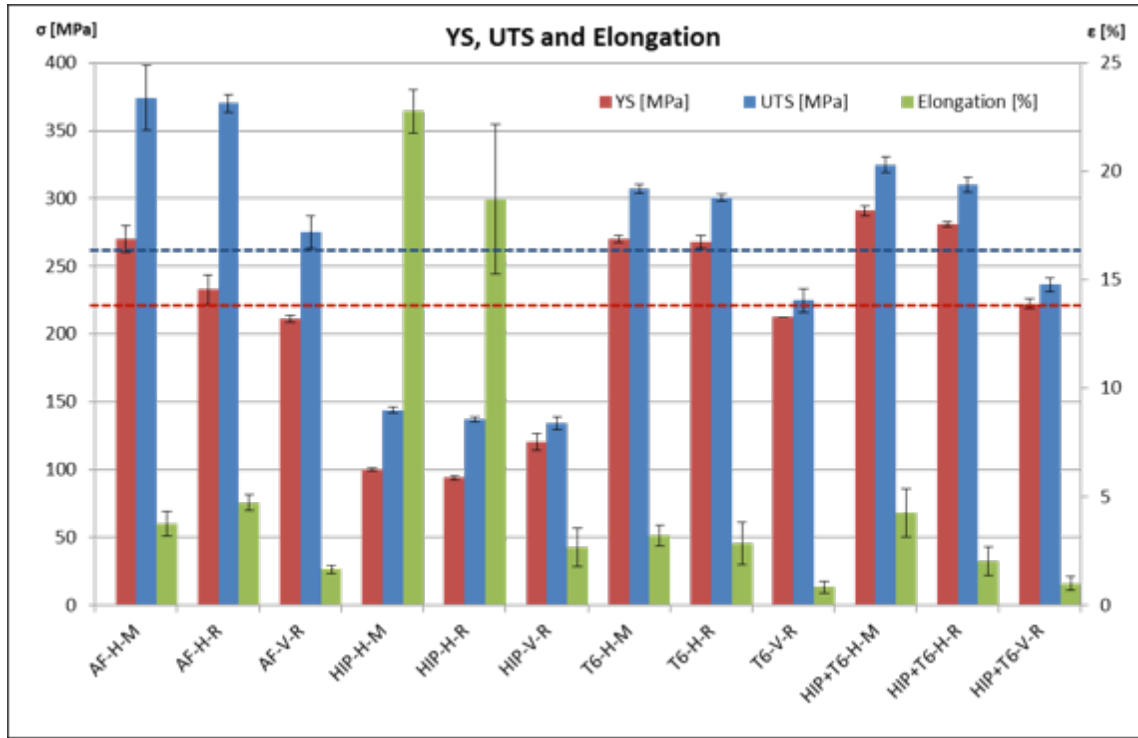


**Fig. 11.** The mechanical properties of all conditions (sample code is shown by Table 3). Dashed lines indicate the standard values for cast+T6 AlSi10Mg [32].

The horizontally built samples generally showed ~25% strength more than the vertically-built samples (compare AF-H-R with AF-V-R, T6-H-R with T6-V-R, and HIP+T6-H-R with HIP+T6-V-R). This is attributed to the voids and their specific orientation. In horizontally built samples, the voids are mainly orientated parallel to the tensile stress, not much interacting with the tensile test. In vertically built samples, voids are mainly orientated perpendicular to the tensile stress (Fig. 5), therefore significantly reducing the intact cross section of the samples and leading earlier failure in the tensile test. Other researchers did not found this void type and thus the differences between horizontal and vertical build orientation were there reported to be small [10,11,33].

The results show only a small advantage for the machined samples over samples with as-fabricated surface for all conditions (compare AF-H-M with AF-H-R, HIP-H-M with HIP-H-

R, T6-H-M with T6-H-R and HIP+T6-H-M with HIP+T6-H-R). For all post-processed conditions, the difference of YS and UTS in favour of machined samples was insignificant ( $\sim < 10$  MPa). This is linked to the as-fabricated surface generally having more irregularities, acting as crack initiation sites. For the machined surface condition, large voids cut open during machining, acting as crack initiation sites. This leads to large scatter in UTS of as-fabricated machined samples (e.g. AF-H-M vs. AF-H-R). The  $\mu$ CT results for the as-fabricated dogbone sample showed a reduced void content in the outer region close to the surface (Fig. 5). The lower void content in the volume close to the sample surface (Fig 5a.) is linked to the additional laser heating for the perimeter of each layer. Machining removes this region, therefore increasing the percentage of void content in the machined samples compared to as-fabricated samples.

Furthermore, samples made from recycled powder show reduced mechanical properties (YS, UTS and elongation), compared against samples made from fresh powder (Fig. 12). Recycled powder was collected from the build chamber and overflow after SLM under Argon atmosphere down to 0.5% Oxygen, briefly stored in cans, and fully re-used (i.e. no fresh powder was added). This reduction is attributed to increased oxide film void content (Fig. 7). The oxide layer voids are yielded by a higher Oxygen content in the recycled powder due to powder being exposed to atmosphere for longer. This is in contrast to reports on other alloys (Ni, Ti), where reactivity with Oxygen is low (at RT), and no such mechanical properties drop was found [17,18].

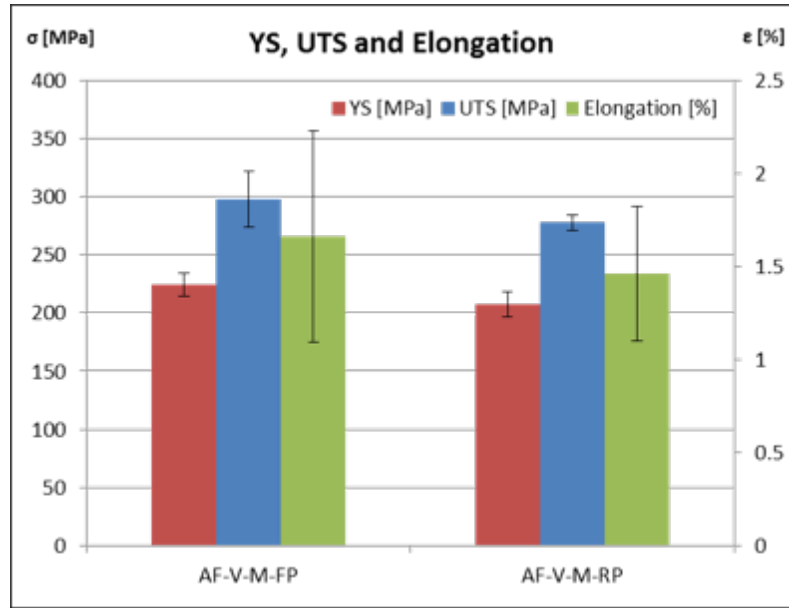


**Fig. 12.** The mechanical properties of vertically built as-fabricated samples processed with fresh powder and 1x recycled powder.

### *III.c. Fractography*

Oxide layers were observed on the as-fabricated fracture surfaces, Fig. 13. Before the tensile test, these oxide layers are present on the void surfaces as shown in Fig. 7. Their orientation on the fractured tensile samples confirms the alignment of the voids with their long axis normal to the build direction.

HIPping was not able to remove the oxide films from the material, but only collapse the oxide-induced void (Fig. 10a). This is proven by the oxide films found on fractured HIP+T6 tensile specimens (Fig. 14d). However, the higher UTS in the HIP+T6 samples over the T6 only samples is still probably linked to HIPping. It can be seen on the fracture surfaces that the HIPped samples showed relatively less oxide films and opened-up voids (comparing Fig. 14b to Fig. 14d). Generally, HIPping can collapse voids, however voids with oxide film on the surface can be still be viewed on fracture surfaces in HIPped samples. Some oxide films within the material might be disrupted and broken by the plastic deformation during HIPping

closing the internal voids, allowing the material to be consolidated, where the Al surfaces can bond without oxide interference, thus increasing the mechanical properties. The fractographs revealed that irregular shaped voids remain in T6-only samples, whereas the voids were removed in the HIPped samples (Fig. 14). However, the oxide surfaces (Fig. 14c) remain in the material.

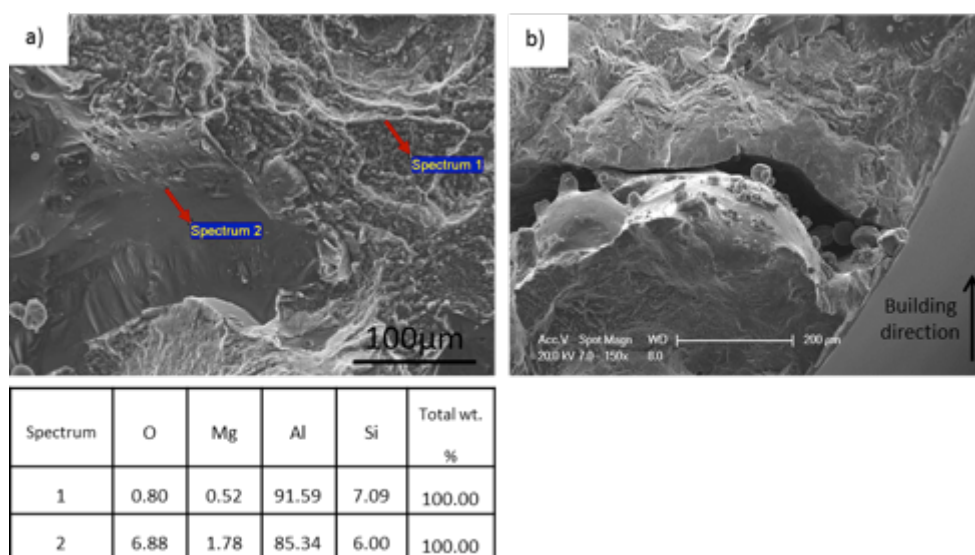


**Fig. 13.** Fractographs of the as-fabricated samples, showing (a) EDX on the fractured surface (spectrum 1), and on the black smooth void surface (spectrum 2), and (b) crack initiation site in a horizontally built and machined sample, void cut open to the surface.

The fracture mode in all samples was generally ductile, with differences between the as-fabricated and post processed condition in the fracture surface topography, Fig. 15. The as-fabricated samples show extremely fine roughness (Fig. 13a), with the fracture roughness morphology at high magnification linked to the Si enriched dendrite cell network (compare Fig. 15b,c with Fig. 9c). It is assumed that the as-fabricated samples fail along the dendrite cell network, where the fracture initiates due to the higher hardness of the Si enriched network and its reduced ductility compared to the Al enriched cells. The post-processed samples show ductile microvoid coalescence morphology (MVC), linked to the grain size of the builds due to the elimination of the Si-rich dendritic network following post-processing.



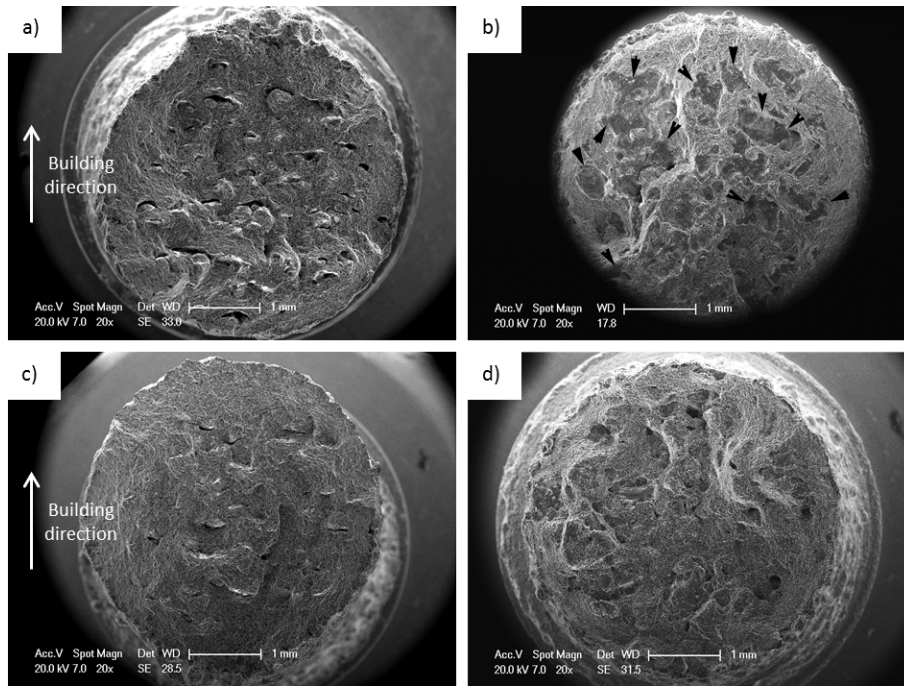


**Fig. 14.** Fractographs showing the void orientation and the effect of HIPping and/or T6: (a) horizontally built T6-only, showing dark elongated voids with their long axis normal to the build orientation, (b) vertically built T6-only sample, showing irregularly-shaped voids and oxide layers (arrowed, corresponding to the smooth feature in Fig. 13a) on the fracture surface, (c) horizontally built HIP+T6 sample showing reduced amount of voids compared with (a), and (d) vertically built HIP+T6 sample, showing reduced amount of voids compared with (b).

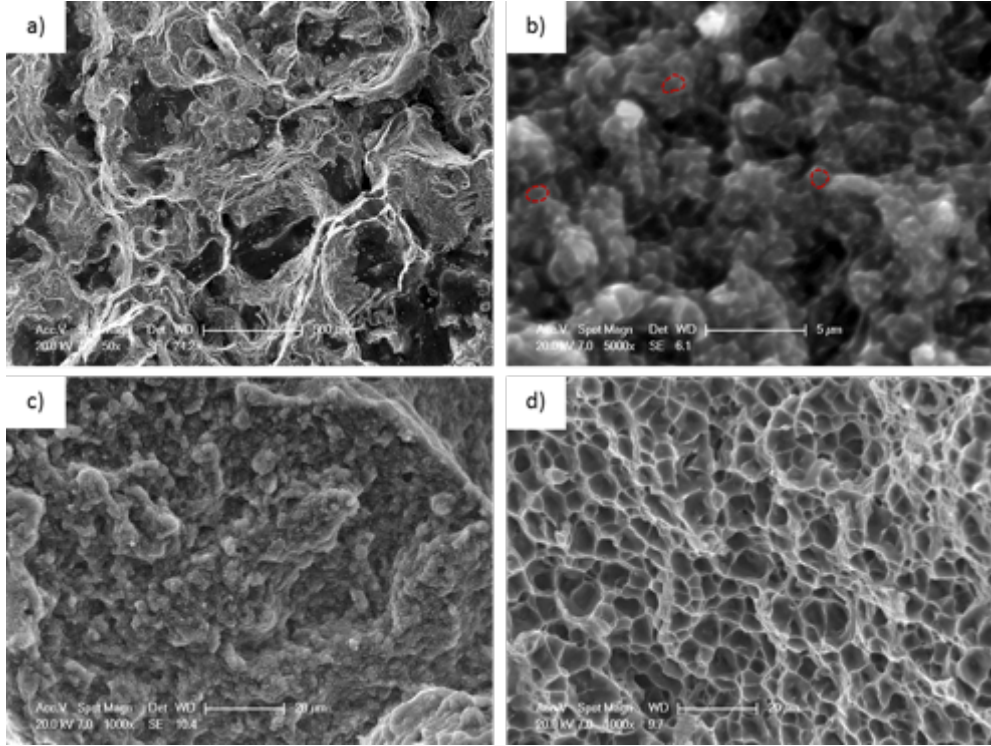


**Fig. 15.** Fractography, surface topography of the different conditions, showing (a) vertically built as-fabricated sample, with deep troughs resembling the meltpool pattern (Fig. 9a.), with oxide films at the bottom of the troughs (as in Fig. 13a), (b) vertically built as-fabricated sample showing failure along the dendrite cell network (Fig. 9c), features of the size of the dendrite cells are exemplary marked by the red dashed lines, (c) vertically built as-fabricated sample showing fine roughness corresponding to the dendrite cell sizes, and (d) HIP-only sample, showing microvoid coalescence.

#### *III.d. Cooling Rate*

The previously described model was used to estimate the cooling rates at different depths below the top surface, Fig. 16. Due to the heat from scan lines either side, there will be additional peaks before and after in time, and variations across the width; just the highest peak at the centre of the scan line has been shown here to illustrate the type of results obtained. Meltpool depths of around  $\sim 100 \mu\text{m}$  were predicted, which correlates well with microstructural observations (Fig. 9-b), with cooling rates of  $5 \times 10^5 - 10^6 \text{ K/s}$ . It was found

that the predictions were particularly sensitive to the latent heat of fusion. Other authors have quoted larger and smaller values that were found to change the predicted cooling rates by +/- 50%. Undercooling and recalescence may additionally significantly affect the actual solidification of this alloy under these AM conditions. So, the model results for behaviour during solidification should be treated with caution currently. The measured cell sizes are consistent with those reported for Al-12Si in CW-SLM [27], although the analysis presented there predicts cooling rates of 1000 K/s for pulsed SLM which are likely to be higher than those for CW-SLM .

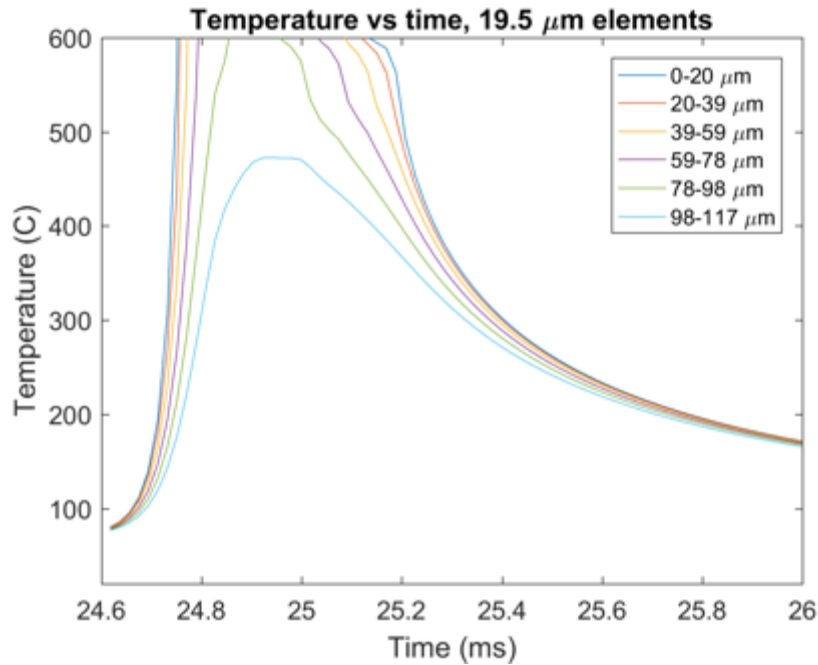


**Fig. 16.** Predicted thermal histories from numerical modelling, using thermophysical properties from [27] which do not include undercooling. The curves show the temperatures predicted at the centres of elements at increasing depths below the top surface as the laser passes over.

It can be seen in Fig. 9 that the pools do not appear to be spaced at 97.5  $\mu\text{m}$  intervals laterally. Two factors may have caused this: firstly the angle of the sample section relative to the laser scanning direction is unknown, but being away from perpendicular would increase the

apparent spacing between the melt pool centres; secondly, the melt pool depth varies considerably across the sample, so deeper pools may well have overwritten the structure of shallower ones. Such variability is not included in the model. These predictions are quite preliminary at this stage, but they provide a useful tool to rationalise the size of the cellular dendritic microstructure observed in the builds.

#### **IV. CONCLUSIONS & FUTURE WORK**

This study rationalised the impact of post-processing on the microstructural and mechanical properties development in AlSi10Mg alloy. As-fabricated samples show a meltpool pattern caused by the SLM scan strategy, with the meltpools consisting of a dendrite cell network with cells  $<1\mu\text{m}$ . Columnar grains were observed along building direction, with equiaxed grains found in-cross section, width and diameter are about  $5\mu\text{m}$  respectively. This development was attributed to the high cooling rates experienced during SLM. The predicted cooling rates during solidification were high ( $>10^5$  K/s). However, they were found to be very sensitive to the heat capacity data used, and there is not yet a clear consensus in the literature on this. Undercooling and recalescence are also very likely to be important.

Furthermore, irregular-shaped voids due to oxide layer formation were observed in the as-fabricated and T6-only condition. It was found that HIPping closes irregular-shaped voids, however oxide layers remain in the microstructure. Post-processed using HIPping or T6 treatment creates a homogenous microstructure with Si particles in an Al matrix. Insignificant grain growth was observed in the HIP+T6 compared with the as-fabricated grain sizes, possibly due to the pinning influence of the various secondary phases.

With regards to the mechanical properties, the as-fabricated, T6-only and HIP+T6 samples show high YS and UTS (above cast+ T6) and small elongation (at the level of cast+T6 alloy). Horizontally built samples were significantly better in YS and UTS than vertically built samples. This is linked to the detrimental void orientation in vertically built samples. Furthermore, samples with a machined surface are better than samples with an as-fabricated surface. This is linked to the reduction of surface defects for machined samples. Generally, ductile fractures were observed in all conditions, with the fracture occurring along the cellular dendritic network in the as-fabricated condition, compared to microvoid coalescence in all the post-processed conditions. Fracture was correlated with oxide film defects.

Future work will focus on the assessment of post-processing on the fatigue behaviour of AlSi10Mg alloys. In-situ, quasi in-situ, and ex-situ experiments combining  $\mu$ CT and mechanical testing will be performed to study the interaction between the oxide film defects and crack propagation.

## **ACKNOWLEDGEMENTS**

Uriel Tradowsky would like to acknowledge the financial support from the Adolf und Lisa Fry Stiftung.

## REFERENCES

1. I. Gibson, D. W. Rosen, and B. Stucker, *Additive Manufacturing Technologies*, 1st ed. (Springer, 2010).
2. P. Reeves, R. Acad. Eng. <http://www.raeng.org.uk/publications/reports/additive-Manufacturing> (2013).
3. L. N. Carter, C. Martin, P. J. Withers, and M. M. Attallah, *J. Alloys Compd.* **615**, 338 (2014).
4. K. Kunze, T. Etter, J. Grässlin, and V. Shklover, *Mater. Sci. Eng. A* **620**, 213 (2015).
5. C. Qiu, G. A. Ravi, and M. M. Attallah, *Mater. Des.* **81**, 21 (2015).
6. L. Thijs, F. Verhaeghe, T. Craeghs, J. Van Humbeeck, and J. P. Kruth, *Acta Mater.* **58**, 3303 (2010).
7. N. Read, W. Wang, K. Essa, and M. M. Attallah, *Mater. Des.* **65**, 417 (2015).
8. K. Kempen, L. Thijs, E. Yasa, M. Badrossamay, W. Verheecke, and J. P. Kruth, *Solid Free. Fabr.* 484 (2001).
9. E. Brandl, U. Heckenberger, V. Holzinger, and D. Buchbinder, *Mater. Des.* **34**, 159 (2012).
10. D. Buchbinder and W. Meiners, Fkz.: 01RIO639A (2011).
11. K. Kempen, L. Thijs, J. Van Humbeeck, and J.-P. Kruth, *Phys. Procedia* **39**, 439 (2012).
12. L. Thijs, K. Kempen, J. P. Kruth, and J. Van Humbeeck, *Acta Mater.* **61**, 1809 (2013).
13. E. Sjölander and S. Seifeddine, *J. Mater. Process. Technol.* **210**, 1249 (2010).

14. E. Sjölander and S. Seifeddine, Mater. Sci. Eng. A **528**, 7402 (2011).
15. G. Ran, J. Zhou, and Q. G. Wang, J. Alloys Compd. **421**, 80 (2006).
16. C. S. C. Lei, W. E. Frazier, and E. W. Lee, Jom **49**, 38 (1997).
17. L. C. Ardila, F. Garciandia, J. B. González-Díaz, P. Álvarez, a. Echeverria, M. M. Petite, R. Deffley, and J. Ochoa, Phys. Procedia **56**, 99 (2014).
18. V. Seyda, N. Kaufmann, and C. Emmelmann, Phys. Procedia **39**, 425 (2012).
19. H. P. Tang, M. Qian, N. Liu, X. Z. Zhang, G. Y. Yang, and J. Wang, Jom **67**, 555 (2015).
20. ASTM International, *ASTM D6773-16, Standard Test Method for Bulk Solids Using Schulze Ring Shear Tester* (ASTM, West Conshohocken, PA, 2016).
21. ASTM International, *ASTM D7481-09, Standard Test Methods for Determining Loose and Tapped Bulk Densities of Powders Using a Graduated Cylinder* (ASTM, West Conshohocken, PA, 2009).
22. A. B. Spierings, M. Voegtlin, T. Bauer, and K. Wegener, Prog. Addit. Manuf. (2015).
23. BSI Standards Publication, *BS EN IS O 6892 Metallic Materials — Tensile Testing Part 1: Method of Test at Ambient Temperature* (2009).
24. ASTM International, *E8 / E8M Standard Test Methods for Tension Testing of Metallic Materials* (2013).
25. S. A. Khairallah, A. T. Anderson, A. Rubenchik, and W. E. King, Acta Mater. **108**, 36 (2016).

26. S. Sulaiman and L. Y. Pio, *Inst. Eng. Malaysia* **65**, 55 (2004).
27. R. Chou, J. Milligan, M. Paliwal, and M. Brochu, *JOM* **67**, 590 (2015).
28. C. L. Yaws, *Thermophysical Properties of Chemicals and Hydrocarbons*, 2nd ed. (Gulf Professional Publishing, 2014).
29. N. C. W. Kuijpers, W. H. Kool, P. T. G. Koenis, K. E. Nilsen, I. Todd, and S. Van der Zwaag, *Mater. Charact.* **49**, 409 (2002).
30. S. Belmares-Perales and a. a. Zaldívar-Cadena, *Mater. Sci. Eng. B Solid-State Mater. Adv. Technol.* **174**, 191 (2010).
31. Y. Birol, *J. Alloys Compd.* **513**, 150 (2012).
32. Deutsches Institut für Normung, *DIN EN 1706 Aluminium Und Aluminiumlegierungen - Gussstücke - Chemische Zusammensetzung Und Mechanische Eigenschaften* (2010).
33. I. Rosenthal, A. Stern, and N. Frage, *Metallogr. Microstruct. Anal.* **3**, 448 (2014).